We are IntechOpen, the world's leading publisher of Open Access books Built by scientists, for scientists

6,900
Open access books available

185,000
International authors and editors

200M
Downloads

Our authors are among the

154
Countries delivered to

TOP 1%
most cited scientists

12.2%
Contributors from top 500 universities



WEB OF SCIENCE™

Selection of our books indexed in the Book Citation Index in Web of Science™ Core Collection (BKCI)

Interested in publishing with us?
Contact book.department@intechopen.com

Numbers displayed above are based on latest data collected.
For more information visit www.intechopen.com



Chapter

Intrinsic Carrier Parameters and Optical Carrier Injection Method in High-Purity Diamonds

Ikuko Akimoto and Nobuko Naka

IntechOpen

Abstract

Diamond attracts increasing attentions as a semiconductor, since high-purity synthesized diamonds have become commercially available in these decades. For appropriate design of any devices, the basic carrier transport parameters should be known. However, it has been difficult to determine carrier parameters in diamond, because the controlled doping and Ohmic contact formation have been hard to achieve. In this chapter, a modern experimental method to measure basic carrier parameters, such as the effective mass, scattering times, and mobility of intrinsic diamonds, is introduced. The method, i.e., nanosecond time-resolved cyclotron resonance (TRCR), is applicable to optically injected carriers in intrinsic diamonds without wire connection. Following the key technique of optical carrier injection, detailed analysis methods for the cyclotron resonance spectra are introduced. The extracted basic parameters of diamond are summarized in comparison to those of silicon and germanium in the same group-IV semiconductor family. This is worthy for triggering further ideas in application-oriented researches using widespread materials.

Keywords: effective mass, scattering time, mobility, cyclotron resonance, optical carrier injection

IntechOpen

1. Introduction

Diamond has been an attractive semiconductor in the fields of power electronics [1], valleytronics [2], optoelectronics [3, 4], and quantum information technology [5, 6] in recent years. Such application-oriented studies have been arising from the outstanding values of breakdown voltage, thermal conductivity, carrier mobility, and spin relaxation time in a diamond. This direction is accelerated due to the progress of crystal growth technique by the chemical vapor deposition (CVD) in these decades [7], by which a highly pure diamond becomes commercially available.

To design diamond-based devices, the knowledge of transport parameters, such as effective mass, scattering time, and drift mobility, is necessary. The effective mass is an important parameter in the band theory of a semiconductor, governing the transport properties, density of states, and the phase boundary of high-density carriers. The drift mobility involving the values of the effective mass and scattering time is a direct index of carrier transport. However, in the past when only natural crystals or impurity-rich synthesized crystals were available, limited information

about intrinsic carrier properties had been reported [8–14]. This historical situation is in contrast to the current materials, silicon, and germanium. In silicon or germanium, a cyclotron resonance method played a significant importance to determine the effective masses for doped crystals under activation by light at low temperature in the 1950s [15, 16]. Such accurate measurements at low temperature had been impossible in diamond due to deep dopant states in the wide energy bandgap. Therefore, most of previous measurements were performed at temperatures higher than 80 K, where a carrier transport was limited by phonon scatterings. A part of anisotropic hole masses were obtained from unresolved spectra at higher temperature than 300 K [11, 12]. Information on the electron was much less, because most of the semiconducting diamond was of *p*-type.

Recently, measurements of time-of-flight (TOF) transport [2, 10, 17, 18] and optical transient grating [19, 20] have been performed with the highly pure crystals. However, the measured carrier mobility varied from sample to sample depending on the surface termination condition, the crystal supplier, and experimental conditions. A high-density injection under high electric field, the space charge-limited transport condition under higher dopant concentration, and non-Ohmic contact caused extrinsic effects on transport behaviors. To clarify intrinsic carrier properties in a diamond, a measurement should be achieved at low temperature under a low carrier density.

In this chapter, our recent experimental contributions to clarify the basic and intrinsic carrier parameters in a diamond will be introduced [21–27]. The measurement has been performed by a time-resolved cyclotron resonance method under optical carrier injection in pure diamond crystals. The concept of our measurement is shown in **Figure 1**: carriers are injected optically with ultra-violet laser pulses through the band-to-band transition or exciton creation with an assistance of phonon emission/absorption in the indirect band structure (**Figure 1a**). Although the created exciton is an electrically neutral binding state of electron and hole, free charge carriers are dissociated from excitons via two-body collision of excitons or thermal dissociation as described in Section 3.2. During the long lifetime of the free carriers in the indirect band structure, we can observe the cyclotron resonance under the external magnetic field (**Figure 1b**). Keys to realize our measurements in an intrinsic semiconductor diamond are the optical carrier injection technique and using of highly pure diamond. As in the case of pure silicon [28], which had been applied to a light-triggered thyristor as a successful power device, optical carrier injection is a promising technique to control a carrier density by a sophisticated way. The spectroscopic way of the optical carrier injection in a diamond at device-operating temperature as well as at low temperature will also be introduced.

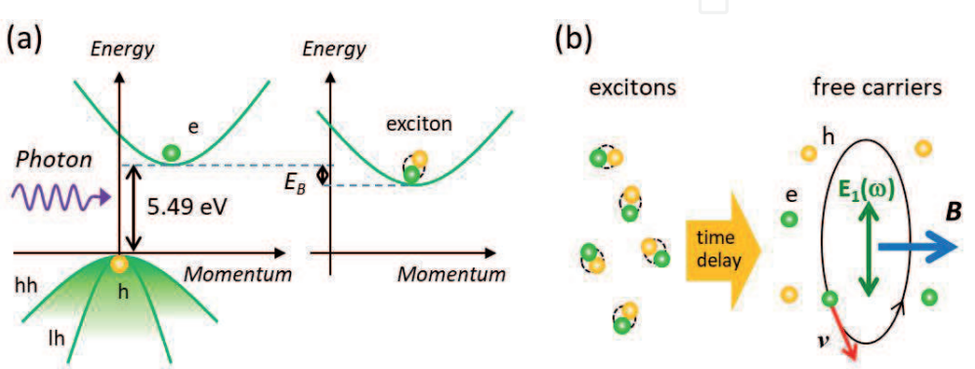


Figure 1.
Schematic experimental concept. (a) Energy diagrams of valence and conduction bands for indirect semiconductor diamond and exciton band and (b) cyclotron motion of optically injected free carriers converted from excitons.

2. Experimental method

The time-resolved cyclotron resonance (TRCR) method was performed for optically injected transient carriers in high-purity diamond crystals in X band (microwave frequency at ν = 9.6 GHz) with a time resolution of a few nanoseconds. The well-resolved CR spectrum can be observed under the condition, $\omega\tau \gg 1$, where $\omega = 2\pi\nu$ is the angular frequency of applied microwave and τ is the carrier scattering time. As the ω is selected by a used equipment, it is necessary to make τ longer by lowering the temperature at cryogenic ones and using pure crystals in order to determine the effective mass in good accuracy.

Highly pure diamond crystals of type-IIIa grown by the CVD method were used. A typical concentration of nitrogen and boron atoms was less than 5 and 1 ppb, respectively ([N] < 9×10^{14} cm^{-3}, [B] < 2×10^{14} cm^{-3}). For crystals of higher impurity concentration, it was difficult to obtain the TRCR spectrum at 10 K because of the broader spectral width due to the higher carrier scattering rate. A typical crystal dimensions were of $3 \times 2 \times 0.5$ mm^3 with the largest plane of the crystalline (001). A crystal was attached on a 2×8 mm^2 face of a right-angle prism by a small amount of vacuum grease for better coupling with the optical excitation (see **Figure 2a**). The sample was mounted in a dielectric microwave cavity (Bruker, MD5W1, TE_{011}) that is developed for the pulsed electron paramagnetic resonance (EPR) in X band with a high filling factor, in which a microwave's electric field packed in a round mode resonates with the cyclotron motion of free carriers under an external magnetic field.

The sample was irradiated by 5-ns pulses at wavelength selected in the range from 219.4 to 226.4 nm at low temperatures or from 219.4 to 235.6 nm at room temperature from an optical parametric oscillator (Spectra Physics, MOPO with frequency doubler option) pumped by THG of a Nd:YAG laser. Temporal responses of continuous microwave power were measured in a quadrature

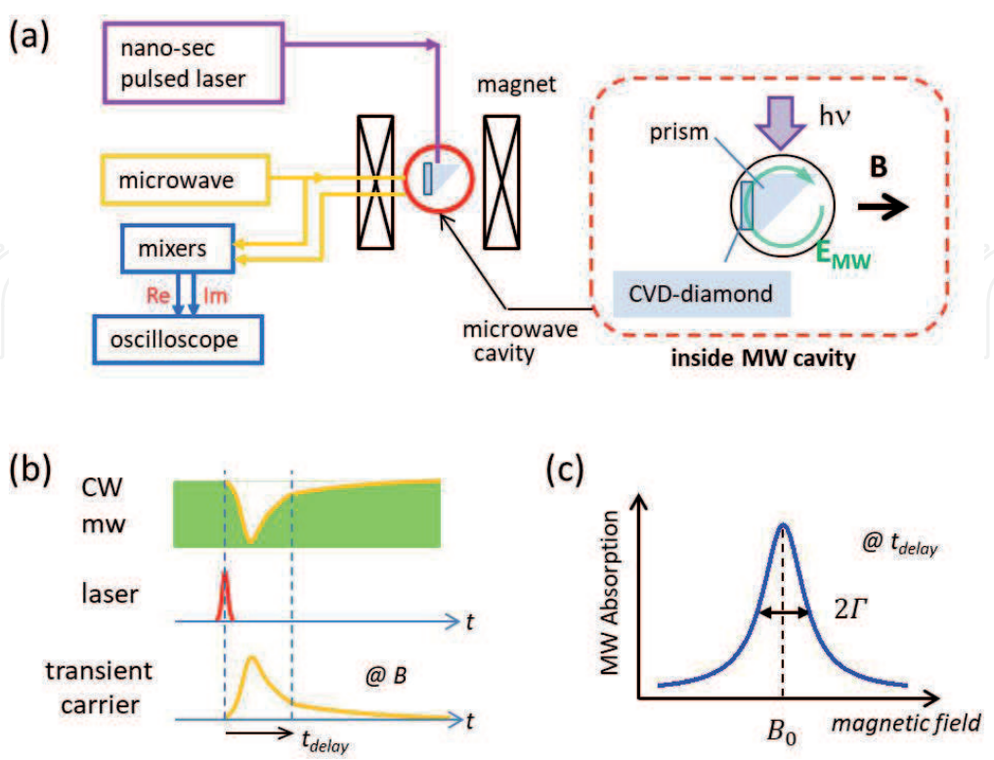


Figure 2.
Schematic drawings of experimental method: (a) the equipment and inside of a microwave cavity, (b) a temporal response of continuously applied microwave to transiently generated carrier by laser pulse at an external magnetic field, and (c) an example of a CR peak in spectrum at a delay time.

detection using microwave mixers and a two-channel oscilloscope of a system (Bruker, ELEXSYS E580) (**Figure 2b**). Inphase and out-of-phase signals to the input microwave were obtained as real and imaginary parts. The cavity's quality factor Q was set at less than 800, corresponding to a time resolution of less than 13 ns by a formula, $\Delta t = Q/\omega$. By sweeping the external magnetic field step-by-step, we obtained the set of the temporal response curves, from which a CR spectrum at a delay time was extracted as a function of the magnetic field as described in Section 3.1. Excitation spectra were also obtained by measuring the signal intensity at an external magnetic field as a function of the excitation wavelength at 10, 80, and 300 K. Although the CR spectrum was too broad to resolve any carrier species at higher temperatures, the amount of free carrier was estimated from the intensity of temporal response under the magnetic field. In addition, the signal intensity was measured according to the rise of temperature.

Important carrier parameters were extracted from a resonance peak in the CR spectrum (**Figure 2c**): the effective mass m^* from the resonance magnetic field B_0 by $m^* = eB_0/\omega = eB_0/2\pi\nu$, the carrier scattering time τ from the spectral half width at half maximum Γ by $1/\tau = \omega\Gamma/B_0$, and carrier drift mobility $\mu = e\tau/m^*$, where e is the elementary charge of electron. The carrier scattering time is also called as momentum relaxation time. For the analysis of effective masses, CR spectra were measured as a function of the magnetic field orientation, where the crystal was rotated about [1–10] crystalline axis so that the external magnetic field was oriented in the (1–10) plane or rotated about [100] axis with the external magnetic field in the (100) plane. Temperature dependence of CR spectral width provides the aspects of carrier scattering mechanism.

In addition to the abovementioned parameters, although we will not describe details here, important properties of carrier generation and decay can be unveiled from the time-resolved cyclotron resonance method: analysis of the rise time of the temporal curve and the signal intensity depending on excitation laser intensity can reveal a carrier generation mechanism [22, 29]. A lifetime of the carrier in a rotating motion is extracted from the decay time of a temporal curve. Temporal variation of carrier density is also estimated based on the plasma shift analysis [16, 30, 31]. Here, to study the basic properties of carriers, we paid careful attention to minimize plasma shifts of the resonance peaks, with the incident pulse energy less than 5.8 μJ which ensures the carrier density at the delay times later than 600 ns is less than 10^{11} cm^{-3}.

3. Results

3.1 Time-resolved cyclotron method

Figure 3a shows a colored contour map of a real part of TRCR signal measured at 7.3 K excited by laser pulses at photon energy of 5.50 eV. Temporal profiles at the magnetic fields of 0.089, 0.122, 0.162, and 0.230 T are shown in **Figure 3b**. CR spectra at the delay times of 60, 200, and 600 ns are shown in **Figure 3c**, by slicing the data set at the delay times. The magnetic field was applied to an angle of 40° from the crystal axis of [001] in the (1–10) plane. In this orientation, four carrier species, light hole, heavy hole, and two electrons in inequivalent conduction valleys, indicated by lh, hh, e1, and e2, respectively, were distinguishable as shown in **Figure 3a** and **c**.

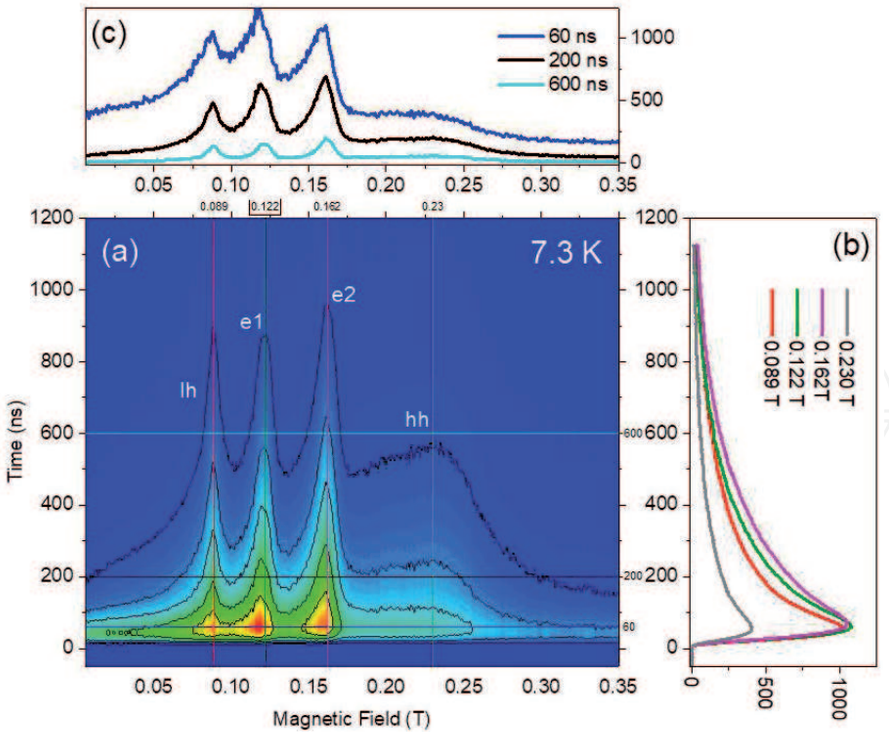


Figure 3.
(a) A colored contour map of a real part of TRCR signal at 7.3 K excited by laser pulses of photon energy at 5.50 eV; (b) temporal profiles at 0.089, 0.122, 0.162, and 0.230 T denoted by vertical lines in (a); (c) CR spectra at the delay times of 60, 200, and 600 ns denoted by horizontal lines in (a).

3.2 Optical carrier injection

Optical carrier injection is a key technique in our nanosecond TRCR method. As a diamond has an indirect band structure as shown in **Figure 1a**, the optical carrier injection at the lowest photon energy is established with the assistance of phonon emission/absorption to satisfy the energy and momentum conservations. The lowest excited state is an exciton band located below the indirect band edge by a binding energy larger than 80 meV [32, 33], whose fine structures were recently clarified [34]. To clarify the spectroscopic way of carrier injection, an excitation spectrum of TRCR signal at the fixed resonant magnetic field was measured with a thin CVD crystal of 70-μm in thickness to suppress the saturation by exciton absorption.

Figure 4 shows the TRCR excitation spectra obtained at 10, 80, and 300 K. The signals were averaged at the time windows, (a) 80–280 ns at 10 K, (b) 352–552 ns at 80 K, and (c) 156–356 ns at 300 K, after the signal decayed to the 1/e of the peak intensity [26]. For such late times, we observed that carriers were dominantly generated by dissociation of excitons [27]. The onset energy of the excitation spectra (a, b) at 5.493 eV coincides with the exciton generation edge assisted by emission of a transverse acoustic (TA) phonon ($E_{ex} + \hbar\omega_{TA}$), where E_{ex} = 5.406 eV is the exciton energy and $\hbar\omega_{TA}$ = 87 meV is the TA phonon energy [35] (see the inset). The second onset at 5.547 eV is assigned to exciton generation assisted by emission of a transverse optical (TO) phonon ($E_{ex} + \hbar\omega_{TO}$), where $\hbar\omega_{TO}$ = 141 meV is the TO phonon energy [35]. Therefore, in the range of the excitation photon energy above 5.493 eV, free carriers can be generated via excitons that are generated by the assistance of phonon emission. At the lower temperatures as 10 K, free carriers were generated by two-body collision of excitons, as the CR signal intensity was proportional to the square of excitation intensity [22].

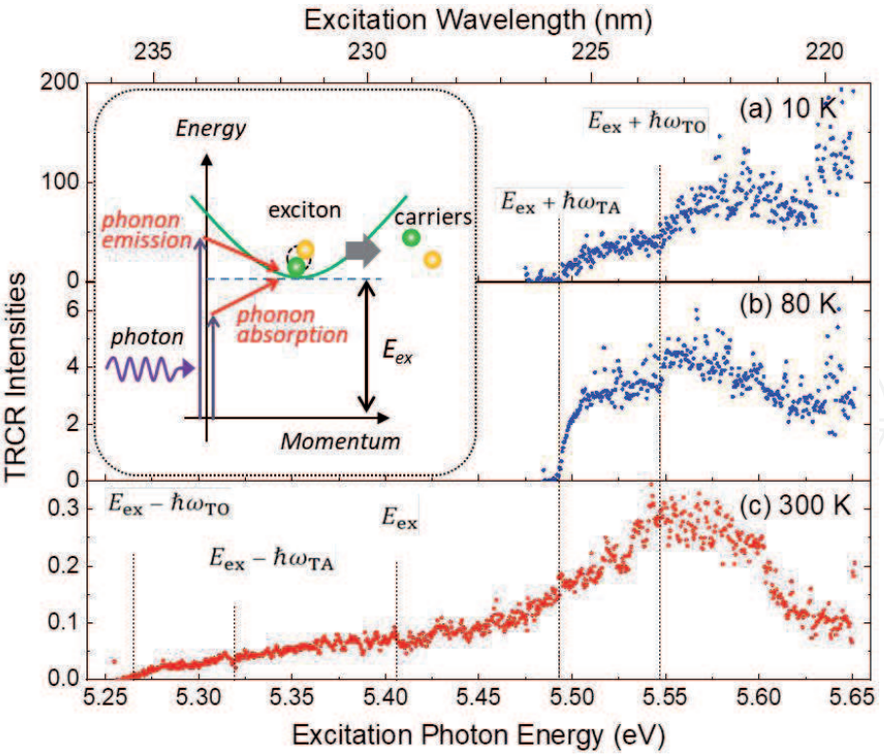


Figure 4.
CR excitation spectra at (a) 10 K, (b) 80 K, and (c) 300 K. Vertical broken lines indicate the energy positions of $E_{ex}\pm\hbar\omega_{TA}$, $E_{ex}\pm\hbar\omega_{TO}$, and E_{ex}. The inset shows schematic of phonon-assisted transitions to the exciton band. This figure was taken from [26] with a slight modification.

On the other hand, the signal at 300 K arose at the lower energy side with the onset at 5.265 eV. The onset energy coincides with the threshold for exciton generation assisted by absorption of a TO phonon ($E_{ex} - \hbar\omega_{TO}$) (see the inset). The onset energy for TA phonon absorption ($E_{ex} - \hbar\omega_{TA}$) is higher as indicated by the vertical broken line (the second one from the left) in **Figure 4c**. In the range of the excitation photon energy from 5.265 to 5.493 eV, free carriers can be generated only at higher temperatures via excitons that are generated by the assistance of phonon absorption. As the CR signal intensity measured at 300 K was proportional to the excitation intensity, the carriers are generated dominantly via a one-body process, such as thermal ionization of excitons [26].

Under the excitation in the range from 5.265 to 5.493 eV, where only the phonon absorption assists the process, the carrier number should increase with rising of the temperature according to the activation of phonons. The lower panel of **Figure 5** shows temperature dependence of the temporal response intensity excited by laser pulse at 5.335 eV. Solid curves in the upper panel are the temperature dependence of the quantum statistical numbers $\langle n\rangle = 1/\left(\exp\left(\hbar\omega_i/k_BT\right) - 1\right)$ of TA and TO phonons, where $\hbar\omega_i$, k_B, and T are the phonon energies for $i = TA$ or TO, Boltzmann constant, and temperature, respectively. The observed signal intensity rose around 150 K in coincidence to the appearance of TA phonon. This suggests that the phonon-assisted optical carrier injection is effective at device-operating temperatures.

In the subsequent Sections 3.3–3.5, we focus on the carrier properties at temperatures below 50 K. This temperature range is uniquely reached by our method owing to the optical carrier injection without the need of thermal activation of carriers from deep levels. For an efficient carrier generation at these temperatures, the excitation wavelength was chosen in the range of 219.4–226.4 nm. Furthermore, we discuss the CR spectra at the later delay times after 600 ns (see **Figure 3**) by eliminating the plasma shift effect at the earlier delay times depending on experimental conditions [16, 31].

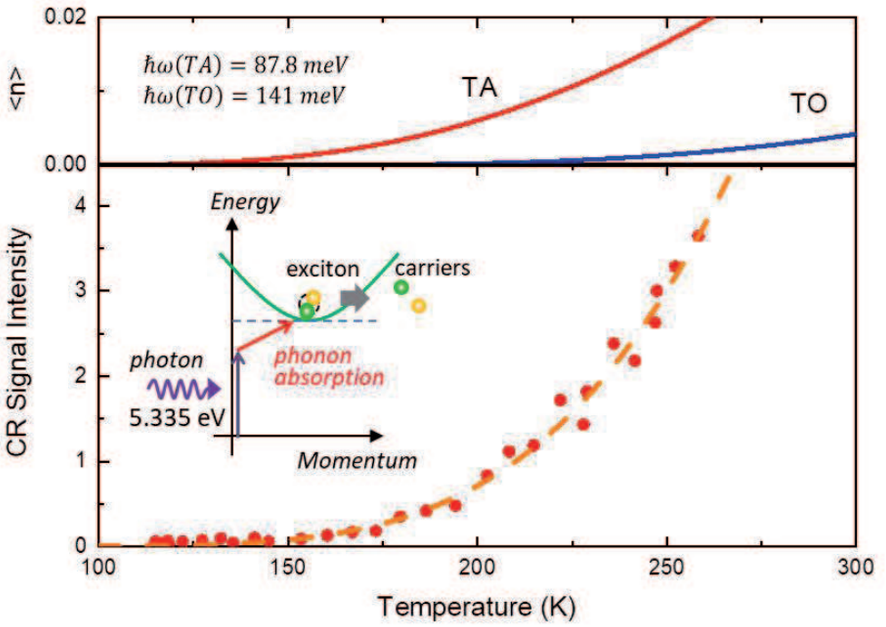


Figure 5.
Temperature dependence of the temporal response signal intensity at 0.16 mT due to free carriers generated by laser pulse at 5.335 eV via phonon absorption. A broken curve in the lower panel is a guide to eyes. Solid curves in the upper panel show the temperature dependence of the quantum statistical number ⟨n⟩ of TA or TO phonon.

3.3 Determination of effective masses

Both CR spectra of real and imaginary parts were well fitted by the formula for the complex conductivity [15]:

$$S(B) = \sum_j \frac{1 - iB_j/\Gamma_j}{\left\{(1 - iB_j/\Gamma_j)^2 + B^2/\Gamma_j^2\right\}}, \tag{1}$$

where Γ_j is a half width and B_j is a central magnetic field at the resonance taken to be common for both real and imaginary parts, B is an external magnetic field, and j represents each resonant component ($j = lh, hh, e1, e2$). We can obtain the effective mass m_j^* and momentum relaxation time τ_j from these fitting parameters by using the relations, $m^* = eB_0/\omega$ and $1/\tau_j = \omega\Gamma_j/B_j$. **Figure 6** plots the extracted effective masses m_j^* at the magnetic field orientations: the positive angles indicate the magnetic field in the (1–10) plane for the rotation axis along [1–10], whereas the negative angles indicate the magnetic field in the (100) plane for the rotation axis along [100].

The effective masses of electrons were simulated according to the following equation [15]:

$$m_{ei}^* = \sqrt{\frac{m_t^2 m_l}{m_t\left(1 - g_i(\theta)^2\right) + m_l g_i(\theta)^2}}, i = 1, 2, 3, \tag{2}$$

where $g_1(\theta) = \pm sin\theta/\sqrt{2}$, $g_2(\theta) = g_3(\theta) = \pm cos\theta$ on (1–10) plane and $g_1(\theta) = \pm sin\theta, g_2(\theta) = \pm cos\theta, g_3(\theta) = 0$ on (100) plane. The curves calculated with parameters $m_t/m_0 = 0.280$ and $m_l/m_0 = 1.560$ [21] trace the data points very well. The curves of e1 and e2 in the (1–10) plane originate from two and four equivalent valleys, respectively. The curve of e2 splits into two curves in the (100) plane, where electron of a constant effective mass is referred as e3.

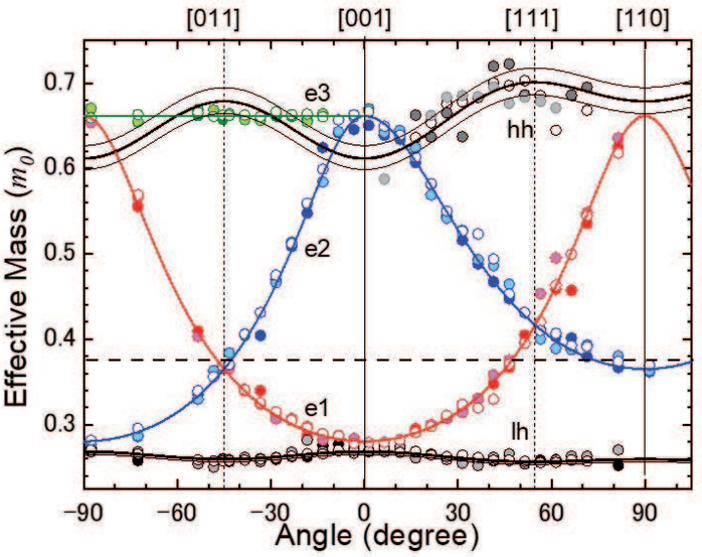


Figure 6.
Angular dependence of effective masses, taken from Ref. [21].

On the other hand, the effective masses of holes were simulated according to the equation for light (−) and heavy (+) holes [15]:

$$m_h^* \sim -\frac{1}{A \pm B'}\left\{1 \pm \frac{1}{A \pm B'}\frac{C^2}{B'}\frac{1}{16}f(\theta)\right\}, \tag{3}$$

where $f(\theta) = \left(1 - 3\cos^2\theta\right)^2/4$ in the (1–10) plane and $f(\theta) = \left(1 - 3\cos^2\theta\sin^2\theta\right)$ in the (100) plane. The thick lines for lh and hh were calculated with parameters $A = -2.670, B' = 1.245, C = 1.898$ [21]. The thin lines are calculated with the upper and lower limit of errors, $\Delta A = \pm 0.020, \Delta B' = \pm 0.025, \Delta C = \pm 0.048$. Moreover, the split-off hole mass calculated from the parameter as $m_{so}/m_0 \approx \hbar^2/(2m_0 A)$ is also plotted by a broken red line. These parameters give band dispersion at the Γ point,

$$E(\boldsymbol{k}) = A k^2 \pm \sqrt{B^2 k^4 + C^2\left(k_x^2 k_y^2 + k_y^2 k_z^2 + k_z^2 k_x^2\right)} \tag{4}$$

with a transformation by $B' = \sqrt{B^2 + C^2/4}$. The finite value of C gives rise to the warping of the valence band.

As we report in detail in Ref. [21], it is experimentally figured out that the electrons are in highly asymmetric valleys along the <001> directions, that is, at the $\triangle$ points, with the transverse effective mass ($m_t = 0.280\, m_0$) and longitudinal effective mass ($m_l = 1.560\, m_0$). And, the doubly degenerate valence-band maxima are located at the Γ point and warping. The values of effective masses were listed in **Table 1** in comparison to those of silicon and germanium [15]. The calculated values of the density of mass for electron $m_{ed} = \left(m_t^2 m_l\right)^{1/3}$ and hole $m_{hd} = \left(m_{lh}^{3/2} + m_{hh}^{3/2} + m_{SO}^{3/2}\right)^{2/3}$ were also listed with the value of direct bandgap energy at Γ point.

Figure 7 compares the angular dependence of effective masses of diamond with those of silicon and germanium [15] with the same angular definition as in **Figure 6**. The conduction-band minimum in silicon is located at the $\triangle$ points as in a diamond, while that in germanium is located at the L points. It is easily recognized that the effective masses in diamond are largest among group-IV semiconductors, reflecting the largest direct bandgap energy at the Γ point which causes relatively larger contribution of the first perturbation term in the **k·p** theory to the effective mass of an energy band.

	E_g^{direct}	m_t	m_l	m_{lh}	m_{hh}	m_{SO}	m_{ed}	m_{hd}
	(eV)				(m_0)			
Ge[a]	0.80	0.082	1.58	0.043	0.336	0.095	0.220	0.378
Si[a]	3.4	0.19	0.97	0.16	0.52	0.23	0.327	0.670
Diamond	7.3	0.280	1.56	0.260	0.667	0.375	0.496	0.947

[a]*Values of germanium and silicon were taken from Ref. [15].*

Table 1.
Comparison of effective mass in group-IV semiconductor.

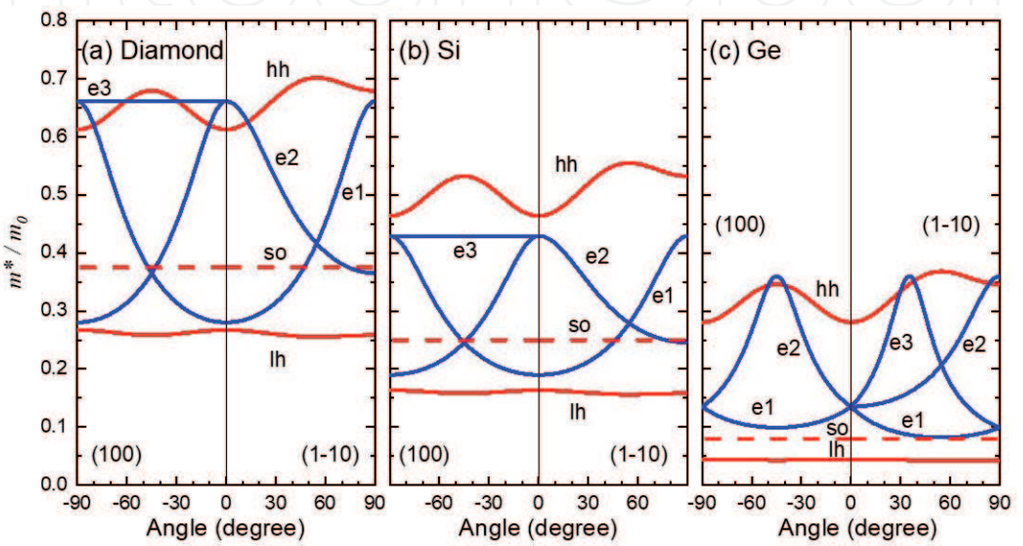


Figure 7.
Comparison of effective mass in group-IV semiconductor: angular dependence of effective masses simulated with the experimentally obtained parameters, in (a) diamond [21], (b) silicon [15], and (c) germanium [15]. Three electrons (blue lines) and light and heavy holes (red lines) are plotted for two rotation planes; the negative angles mean the magnetic field in the (100) plane for the rotation axis along [100], whereas the positive angles mean the magnetic field in the (1–10) plane for the rotation axis along [1–10].

3.4 Sample dependence of carrier lifetime

A well-resolved spectrum of TRCR at the lower temperatures allows extracting the effective masses in good accuracy as described in Section 3.3. We compared the TRCR signals in different samples as reported in Refs. [24, 25]. The sample showed the narrower spectral width as presented in **Figure 3** possesses the smaller concentration of donor and acceptor, that is, nitrogen and boron. **Figure 8** shows temporal profiles of five different samples. The sample displayed a slow rise and decay in a couple of hundred nanoseconds (sample A) which is identical to that in **Figure 3**. The narrow spectral width is caused by the long carrier scattering time. From the comparison of CR spectra of CVD diamonds to those of dislocation-free HPHT diamonds, we found the fact that the TRCR detection is rather insensitive to crystalline dislocations [24]. It is known that a typical dislocation density in CVD diamond is lower than 10^4 cm^{-2} [36], corresponding to dislocation periods larger than 100 μm. On the other hand, the cyclotron radii in the measurement with X band microwave were 86 and 55 nm for light and heavy holes, respectively. As the carriers rotate in the much smaller spatial extension than the typical dislocation period in CVD samples, the CR detection is rather insensitive to dislocations. Instead, impurity scattering by neutral nitrogen atoms is found to be dominant at low temperatures (as described in Section 3.5), because their average separations are comparable to the cyclotron radii in the present case.

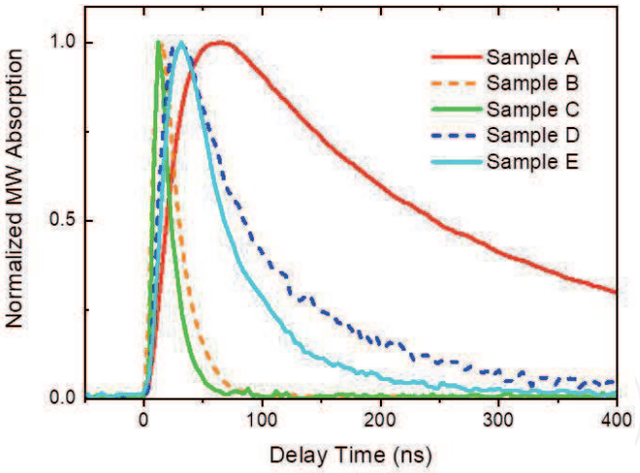


Figure 8.
Temporal profiles at the resonance of light hole in different five samples listed in ***Table 2****, taken from Ref. [25].*

From these facts, we emphasize that the accurate determination of effective masses as described in Section 3.3 became possible, since we could use a highly pure diamond produced by the CVD method under the optical carrier injection.

The rise time and decay time in the temporal profile of TRCR in **Figures 3b** and **8** reveal carrier generation and trapping mechanism. The finite rise time reflects the time required for carrier creation by exciton collision. A detailed formula giving an approximate rise time in connection with the lifetime is described in Refs. [22, 29]. The shorter decay time is probably caused by the higher density of impurity concentrations (in comparison among samples A–C) and by the higher density of stacking faults and substitutional impurities (in comparison samples E–D). It has been known that incorporation of defects occurs more easily in a (111)-oriented diamond than in an (001)-oriented diamond.

3.5 Carrier scattering time and drift mobility

The temperature dependence of TRCR spectrum provides the aspect of carrier scattering mechanisms. **Figure 9a** shows the normalized temporal curves measured at 0.16 mT at various temperatures. The rise time and the decay time of the signal increased as the temperature is rising. The longer rise and decay times at higher temperatures indicate elongating of the carrier lifetime [22]. This is probably caused by trapping of carriers into impurity states at lower temperatures. Similar shortening of the exciton lifetime at low temperatures was clarified in Ref. [37] by comparing exciton lifetimes in samples containing different concentrations of impurities.

Sample	Growth	Boron	Nitrogen	Dislocation
A	CVD (001)-sector	<1 ppb	<5 ppb	–
B	CVD (001)-sector	<50 ppb	<100 ppb	–
C	HPHT+neutron irrad.	–	51 ppm	–
D	HPHT (001)-sector	<0.8 ppb	<45 ppb	Free
E	HPHT (111)-sector	<0.8 ppb	<45 ppb	Free

"-" means unknown.

Table 2.
Specification of used samples.

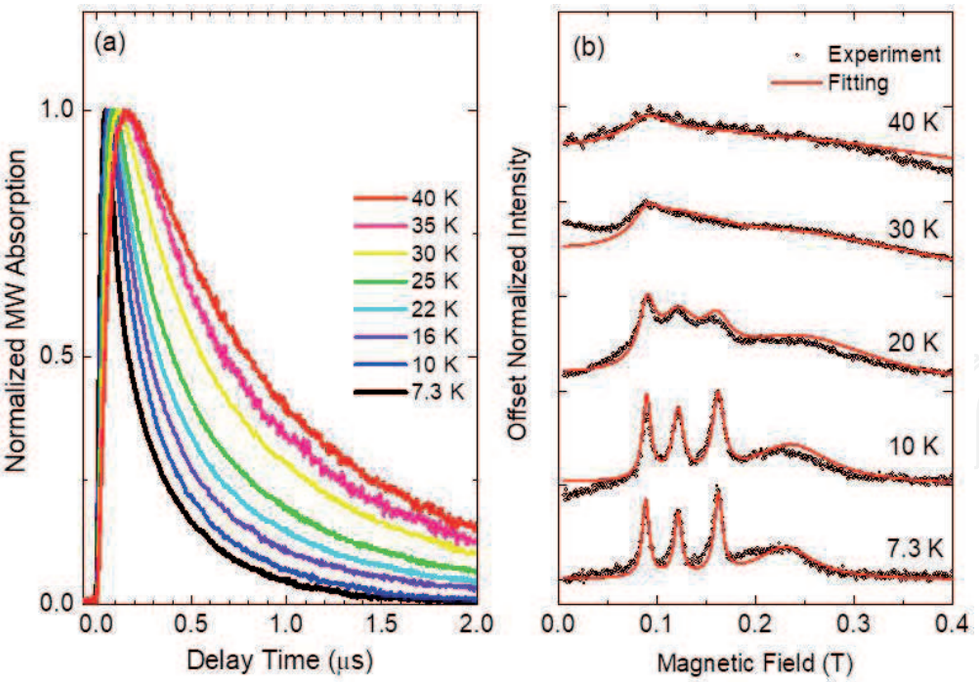


Figure 9.
Temperature variation of temporal curves at 0.16 mT (a) and spectrum at the delay time 1 μs averaged for ±40 ns (b), adapted from Ref. [23].

Figure 9b shows the CR spectra at 7.3, 10, 20, 30, and 40 K taken at a delay time of 1 μs after the laser pulse with averaging window for ±40 ns [23]. The four peaks were separately observed up to 20 K and the width broadened with increasing temperature. These spectra were analyzed by the abovementioned spectrum fitting. The carrier scattering times τ_j's, in other words, momentum relaxation times, were taken from the width Γ_j as a function of temperature. The fitting of the structureless spectra at the higher temperatures was possible by fixing the resonance field of the four components. The fitting curve of each spectrum is shown by the thin red lines.

The spectral width Γ_j at low temperature sharply depends on the impurity concentration as mentioned in Section 3.4. The carrier scattering at low temperature is mainly governed by the neutral impurity scattering instead of the ionized impurity, because the optically injected carriers neutralize ionized impurity centers. **Figure 10a** shows the temperature dependence of the inverse carrier scattering times $1/\tau_j$ extracted from the spectra measured with a CVD diamond shown in **Figure 9b**. The data points are well reproduced by the sum of the longitudinal acoustic (LA) phonon scattering rate $1/\tau_{acj}$ and a constant term b_j (solid lines). The LA phonon scattering rate $1/\tau_{acj}$ (broken lines) was calculated for electrons and holes by using Eq. (6) in Ref. [38] with a deformation potential of 8.7 eV [35] (6.8 eV) for e1 (e2) electrons or 10.0 eV for both types of holes in diamond. Deviation from the straight line of the $T^{3/2}$ law which was known for acoustic phonon scattering appeared below 40 K due to inhibition of LA phonon emission at low temperatures. The constant terms were attributed to neutral impurity scattering rates. The best fit values were $b_{e1} = 1.4 \times 10^9\,s^{-1}$, $b_{e2} = 1.3 \times 10^9\,s^{-1}$, $b_{lh} = 2 \times 10^9\,s^{-1}$, and $b_{hh} = 8 \times 10^9\,s^{-1}$. As discussed in Ref. [23], these values were larger than the values calculated by modified Erginsoy's formulas, $\beta_e = (3.4 n_A a_A + 20 n_D a_D)\hbar/m_e^*$ for the electron [39] and $\beta_h = (20 n_A a_A + 3.4 n_D a_D)\hbar/m_h^*$ for the hole, where $a_{A(D)}$ is a Bohr radius and $n_{A(D)}$ is the concentration of acceptors (donors). This fact indicates that the estimated $n_I a_I$ $(I = A, D)$ were smaller than those in the actual situations probably owing to the too much simplified estimation of the Bohr radius by the hydrogenic model.

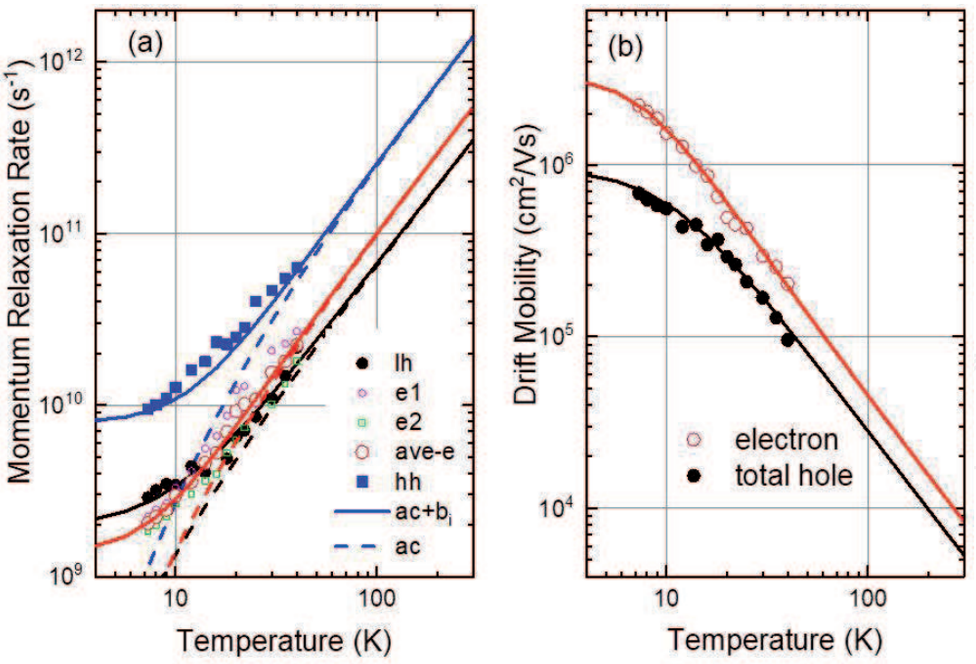


Figure 10.
Temperature dependences of carrier scattering time (a) and drift mobility (b), taken from Ref. [23].

	Mobility at 300 K (cm^2/Vs)	
	μ_e	μ_h
Ge	3900[a]	1900[a]
Si	1450[a]	500[a]
Diamond	7300[b]	5300[b]

[a]*Taken from Ref. [42].*
[b]*Present extrapolated values.*

Table 3.
Comparison of mobility at 300 K.

Now as the parameters of the effective mass m^* and carrier scattering time τ were individually obtained from the analysis of CR spectra, we can derive the drift mobility by the relation $\mu = e\tau/m^*$. **Figure 10b** shows the drift mobilities of electron and hole. We used a conductivity mass for the electron, $m_e^* = 3/(1/m_l + 2/m_t) = (0.386 \pm 0.026)\, m_0$. For the valence bands, effective masses were averaged for the warped energy surfaces $m_{lh}^*/m_0 = 0.261 \pm 0.005$ for the light hole and $m_{hh}^*/m_0 = 0.663 \pm 0.032$ for the heavy hole. The total hole mobility was obtained by weighting the light and heavy hole mobilities as $\mu = (p_{lh}\mu_{lh} + p_{hh}\mu_{hh})/(p_{lh} + p_{hh}) = (\mu_{lh} + r\mu_{hh})/(1 + r)$ with the ratio $r = p_{hh}/p_{lh} = (m_{hh}/m_{lh})^{3/2} = 4.05$ derived from the density-of-state ratio for the degenerate energy bands [40]. The drift mobility at 10 K was obtained as $\mu_e = (1.52 \pm 0.27) \times 10^6\,\mathrm{cm^2/Vs}$ for electrons and $\mu_{lh} = (2.26 \pm 0.38) \times 10^6$ and $\mu_{hh} = (0.24 \pm 0.03) \times 10^6\,\mathrm{cm^2/Vs}$ for the light and heavy holes. The ratio of light to heavy hole mobilities $\mu_{lh}/\mu_{hh} \cong 9.35$ is in better agreement with the ratio of $(m_{hh}^*/m_{lh}^*)^{5/2} = 10.3$ than $m_{hh}^*/m_{lh}^* = 2.54$. This fact indicates that light and heavy holes in ultrapure diamond relax inside each band. This is in contrast to the case in p-type germanium [40], where the intra-/inter-band scattering is dominant for the heavy-/light-hole and then μ_{lh}/μ_{hh} is proportional to m_{hh}^*/m_{lh}^*.

We evaluated the mobility up to 300 K by extrapolating the $T^{3/2}$ relation as shown by the solid lines, because the optical phonon process dominates carrier

scattering only above 400 K in diamond [41]. The values of the mobility at 300 K were derived as μ_e = 7.3 × 10^3 cm^2/Vs for electron and 5.3 × 10^3 cm^2/Vs for total hole. The values are higher than those evaluated by Reggiani et al. [8] and Nava et al. [9] for a natural n(p)-type diamond crystal or by Isberg et al. [10, 17] with the CVD diamond crystals. The values are summarized in **Table 3** in comparison to those in silicon and germanium at 300 K [42]. The highest mobility of both electron and hole responsive to 10 GHz at 300 K indicates the outstanding possibility of a diamond in the field of power electronics and optoelectronics.

4. Conclusion

Recently developed experimental method, the nanosecond time-resolved cyclotron resonance, was introduced to clarify the basic carrier transport parameters in an intrinsic diamond. A sophisticated optical carrier injection technique in a highly pure diamond crystal realized the measurement at low temperature. The extracted effective masses, carrier scattering times, and mobilities unveiled the supreme carrier transport properties of a highly pure diamond, which indicate a large application-oriented advantage especially in power electronics and optoelectronics fields. The introduced optical carrier injection is a promising technique to control a carrier density in future devices.

Acknowledgements

The authors thank J.H. Kaneko (Hokkaido University) for providing the diamond sample grown by the CVD method and Ms. S. Hamabata (Wakayama University) for the experiments described in Section 3.2. This work was supported by JSPS KAKENHI (Grant Nos. 15 K05129 and 17H02910) and the Murata Science Foundation.

Author details

Ikuko Akimoto[1*] and Nobuko Naka[2]

1 Wakayama University, Wakayama, Japan

2 Kyoto University, Kyoto, Japan

*Address all correspondence to: akimoto@sys.wakayama-u.ac.jp

IntechOpen

© 2019 The Author(s). Licensee IntechOpen. This chapter is distributed under the terms of the Creative Commons Attribution License (http://creativecommons.org/licenses/by/3.0), which permits unrestricted use, distribution, and reproduction in any medium, provided the original work is properly cited. CC BY

References

[1] Hiraiwa A, Kawarada H. Figure of merit of diamond power devices based on accurately estimated impact ionization processes. Journal of Applied Physics. 2013;**114**:034506. DOI: 10.1063/1.4816312

[2] Isberg J, Gabrysch M, Hammersberg J, Majdi S, Kovi KK, Twitchen DJ. Generation, transport and detection of valley-polarized electrons in diamond. Nature Materials. 2013;**12**:760. DOI: 10.1038/NMAT3694

[3] Makino T, Yoshino K, Sakai N, Uchida K, Koizumi S, Kato H, et al. Enhancement in emission efficiency of diamond deep-ultraviolet light emitting diode. Applied Physics Letters. 2011;**99**:061110. DOI: 10.1063/1.3625943

[4] Breeze JD, Salvadori E, Sathian J, Alford NM, Kay CWM. Continuous-wave room-temperature diamond maser. Nature. 2018;**555**:493. DOI: 10.1038/nature25970

[5] Kosaka H, Niikura N. Entangled absorption of a single photon with a single spin in diamond. Physical Review Letters. 2015;**114**:053603. DOI: 10.1103/PhysRevLett.114.053603

[6] Weber JR, Koehl WF, Varley JB, Janotti A, Buckley BB, Van de Walle CG, et al. Quantum computing with defects. PNAS. 2010;**107**:8513. DOI: 10.1073/pnas.1003052107

[7] Balmer RS, Brandon JR, Clewes SL, Dhillon HK, Dodson JM, Friel I, et al. Chemical vapour deposition synthetic diamond: Materials, technology and applications. Journal of Physics. Condensed Matter. 2009;**21**:364221. DOI: 10.1088/0953-8984/21/36/364221

[8] Reggiani L, Bori S, Canali C, Nava F, Kozlov SF. On the lattice scattering and effective mass of holes in natural diamond. Solid State Communications. 1979;**30**:333. DOI: 10.1016/0038-1098(79)90645-8

[9] Nava F, Canali C, Jacobini C, Reffiani L, Kozlov SF. Electron effective masses and lattice scattering in natural diamond. Solid State Communications. 1980;**33**:475. DOI: 10.1016/0038-1098(80)90447-0

[10] Isberg J, Hammersberg J, Johansson E, Wilstroem T, Twitchen DJ, Whitehead AJ, et al. High carrier mobility in single-crystal plasma-deposited diamond. Science. 2002;**297**:1670. DOI: 10.1126/science.1074374

[11] Kono J, Takeyama S, Takamasu T, Miura N, Fujimori N, Nishibayashi Y, et al. High-field cyclotron resonance and valence-band structure in semiconducting diamond. Physical Review B. 1993;**48**:10917. DOI: 10.1103/PhysRevB.48.10917

[12] Rauch CJ. Millimeter cyclotron resonance experiment in diamond. Physical Review Letters. 1961;**7**:83. DOI: 10.1103/PhysRevLett.7.83

[13] Redfield AG. Electronic hall effect in diamond. Physics Review. 1954;**94**:526. DOI: 10.1103/PhysRev.94.526

[14] Denham P, Lightowlers EC, Dean PJ. Ultraviolet intrinsic and extrinsic photoconductivity of natural diamond. Physics Review. 1967;**161**:762. DOI: 10.1103/PhysRev.161.762

[15] Dresselhaus G, Kip AF, Kittel C. Cyclotron resonance of electrons and holes in silicon and germanium crystals. Physics Review. 1955;**98**:368. DOI: 10.1103/PhysRev.98.368

[16] Dresselhaus G, Kip AF, Kittel C. Plasma resonance in crystals: Observations and theory. Physics Review. 1955;**100**:618. DOI: 10.1103/PhysRev.100.618

[17] Gabrysch M, Majdi S, Twitchen DJ, Isberg J. Electron and hole drift velocity in chemical vapor deposition diamond. Journal of Applied Physics. 2011;**109**:063719. DOI: 10.1063/1.3554721

[18] Majdi S, Kovi KK, Hammersberg J, Isberg J. Hole transport in single crystal synthetic diamond at low temperatures. Applied Physics Letters. 2013;**102**:152113. DOI: 10.1063/1.4802449

[19] Ščajev P, Gudelis V, Ivakin E, Jarašiūnas K. Nonequilibrium carrier dynamics in bulk HPHT diamond at two-photon carrier generation. Physica Status Solidi A: Applications and Materials Science. 2011;**208**:2067. DOI: 10.1002/pssa.201100006

[20] Nesladek M, Bogdan A, Deferme W, Tranchant N, Bergonzo P. Charge transport in high mobility single crystal diamond. Diamond and Related Materials. 2008;**17**:1235. DOI: 10.1016/j.diamond.2008.03.015

[21] Naka N, Fukai K, Handa Y, Akimoto I. Direct measurement via cyclotron resonance of the carrier effective masses in pristine diamond. Physical Review B. 2013;**88**:035205. DOI: 10.1103/PhysRevB.88.035205

[22] Naka N, Fukai K, Handa Y, Akimoto I. Nanosecond cyclotron resonance in ultrapure diamond. Journal of Luminescence. 2014;**152**:93. DOI: 10.1016/j.jlumin.2013.12.055

[23] Akimoto I, Handa Y, Fukai K, Naka N. High carrier mobility in ultrapure diamond measured by time-resolved cyclotron resonance. Applied Physics Letters. 2014;**105**:032102. DOI: 10.1063/1.4891039

[24] Akimoto I, Naka N, Tokuda N. Time-resolved cyclotron resonance on dislocation-free HPHT diamond. Diamond and Related Materials. 2016;**63**:38. DOI: 10.1016/j.diamond.2015.08.013

[25] Naka N, Morimoto H, Akimoto I. Excitons and fundamental transport properties of diamond under photo-injection. Physica Status Solidi A: Applications and Materials Science. 2016;**213**:2551. DOI: 10.1002/pssa.201600237

[26] Hamabata S, Akimoto I, Naka N. Temperature-dependent carrier injection routes under optical excitation in high-purity diamond crystals. Journal of Physics: Conference Series; accepted

[27] Akimoto I, Hamabata S, Kaneko JH, Naka N. in preparation

[28] Akimoto I, Naka N. Two optical routes of cold carrier injection in silicon revealed by time-resolved excitation spectroscopy. Applied Physics Express. 2017;**10**:061301. DOI: 10.7567/APEX.10.061301

[29] Naka N, Akimoto I, Shirai M. Free-carrier generation by two-photon resonant excitation to the excitonic states in cuprous oxide. Physica Status Solidi B. 2013;**250**:1773. DOI: 10.1002/pssb.201200713

[30] Naka N, Akimoto I, Shirai M, Kan'no K. Time-resolved cyclotron resonance in cuprous oxide. Physical Review B. 2012;**85**:035209. DOI: 10.1103/PhysRevB.85.035209

[31] Akimoto I, Torai S, Naka N, Shirai M. Temporal shift from magnetoplasma resonance to cyclotron resonance of photo carriers generated from 1 s-exciton on cuprous oxide crystal. European Physical Journal B. 2012;**85**:374. DOI: 10.1140/epjb/e2012-30618-8

[32] Clark CD, Dean PJ, Harris PV. Intrinsic edge absorption in diamond. Proceedings of the Royal Society A. 1964;**277**:312. DOI: 10.1098/rspa.1964.0025

[33] Dean PJ, Male JC. Luminescence excitation spectra and recombination

radiation of diamond in the fundamental absorption region. Proceedings of the Royal Society A. 1964;**277**:330. DOI: 10.1098/rspa.1964.0026

[34] Hazama Y, Naka N, Stolz H. Mass-anisotropy splitting of indirect excitons in diamond. Physical Review B. 2014;**90**:045209. DOI: 10.1103/PhysRevB.90.045209

[35] Jacoboni C, Reggiani L. The Monte Carlo method for the solution of charge transport in semiconductors with applications to covalent materials. Reviews of Modern Physics. 1983;**55**:645. DOI: 10.1103/RevModPhys.55.645

[36] Martineau PM, Gaukroger MP, Guy KB, Lawson SC, Twitchen DJ, Friel I, et al. High crystalline quality single crystal chemical vapour deposition diamond. Journal of Physics. Condensed Matter. 2009;**21**:364205. DOI: 10.1088/0953-8984/21/36/364205

[37] Naka N, Omachi J, Sumiya H, Tamasaku K, Ishikawa T, Kuwata-Gonokami M. Density-dependent exciton kinetics in synthetic diamond crystals. Physical Review B. 2009;**80**:035201. DOI: 10.1103/PhysRevB.80.035201

[38] Trauernicht DP, Wolfe JP. Drift and diffusion of paraexcitons in Cu_2O: Deformation-potential scattering in the low-temperature regime. Physical Review B. 1986;**33**:8506. DOI: 10.1103/PhysRevB.33.8506

[39] Erginsoy C. Neutral impurity scattering in semiconductors. Physics Review. 1950;**79**:1013. DOI: 10.1103/PhysRev.79.1013

[40] Brown DM, Bray R. Analysis of lattice and ionized impurity scattering in *p*-type Germanium. Physics Review. 1962;**127**:1593. DOI: 10.1103/PhysRev.127.1593

[41] Pernot J, Volpe PN, Omnes F, Muret P, Mortet V, Haenen K, et al. Hall hole mobility in boron-doped homoepitaxial diamond. Physical Review B. 2010;**81**:205203. DOI: 10.1103/PhysRevB.81.205203

[42] Sze SM, Ng KK. Physics of Semiconductor Devices. 3rd ed. New York: Wiley-Interscience; 1981. ISBN-10: 0471143235